International Journal of Heat and Mass Transfer 196 (2022) 123203

Contents lists available at ScienceDirect

International Journal of Heat and Mass Transfer

journal homepage: www.elsevier.com/locate/hmt

Characterization of thermal behavior of a micro pulsating heat pipe by local heat transfer investigation

Naoko Iwata[a,*], Fabio Bozzoli[a,b], Luca Pagliarini[a], Luca Cattani[c], Pamela Vocale[a], Matteo Malavasi[a], Sara Rainieri[a]

[a] Department of Engineering and Architecture, University of Parma, Parma, Italy
[b] SITEIA.PARMA Interdepartmental Centre, University of Parma, Parma, Italy
[c] CIDEA Interdepartmental Centre, University of Parma, Parma, Italy

ARTICLE INFO

Article history:
Received 20 April 2022
Revised 16 June 2022
Accepted 26 June 2022

Keywords:
Pulsating heat pipe
Infrared thermography
Inverse heat conduction problem
Local heat flux

ABSTRACT

The thermal behavior of Pulsating Heat Pipes (PHPs), which is inherently time-dependent, could also significantly change from local position to local position. Hence, the evaluation of local heat flux distributions could lead to a better understanding of the fundamental governing mechanisms of PHPs, which are, so far, only partially understood. In fact, most of the studies regarding the working principles of PHPs have focused on analysing the heat transfer rate averaged over the evaporator and condenser areas, or on evaluating the overall thermal resistance of the system. A 7-turn micro-PHP with an inner diameter of 0.32 mm was charged with HFC-134a at filling ratio of 46% and tested in bottom heated mode. The external wall temperature distribution of the condenser was measured by a high-speed and high-resolution infrared camera. The local heat fluxes exchanged between the fluid and the PHP wall were estimated in the whole condenser by solving the inverse heat conduction problem with the temperature maps as input data. In order to study the PHP working regimes, the local heat transfer behavior was furthermore investigated in terms of characteristic frequencies of the oscillatory flow by means of the wavelet method, coupled with a statistical approach. At low heat input the variations over time and along space of axial coordinate in the heat flux were significant and each tube showed multiple peaks in the power spectrum. On the other hand, the variation weakened under the high heat input conditions and the dominant fluid oscillation frequency was found more clearly around 1.2 Hz. All the qualitative and quantitative pieces of data are comprehensively presented to give further information regarding the device behavior at different heat input.

1. Introduction

Thermal management is critical for several fast-growing markets, such as the lithium-ion battery market, which is expected to register a compound annual growth rate of approximately 22% during the forecast period (2019–2024) [1]. Lithium-ion batteries, which are mainly used for electric vehicle and energy storage systems, should be maintained within a strict temperature range during operation to prevent either losses in performance or thermal runaways [2]. In addition, the widespread introduction of microelectronics in almost every processing line had led to the critical thermal issues of the high heat density of microprocessor chips [3]. In fact, a high operating temperature reduces the reliability and performance of electronics, and eventually causes fatal failure. Thus, the thermal management of complex electronic systems has become an important challenge.

Two-phase thermal devices are more efficient than single-phase devices because some or all of the heat transport occurs via latent heat. A Pulsating Heat Pipe (PHP), also known as an Oscillating Heat Pipe, was invented by Akachi in the 1990s [4–6] and is a promising two-phase passive heat transfer device that consists of a capillary tube or channel that is bent repeatedly between an evaporator and a condenser. The inner diameter of the tube or hydraulic diameter of the channel should be enough small so that the working fluid in the PHP exists as a mixture of liquid slugs and vapor plugs even in a gravity environment. Heat is transferred from the evaporator to the condenser by the self-excited oscillation of slug/plug flow. Compared with other two-phase passive thermal devices, such as conventional heat pipes [7] and loop heat pipes [8], PHPs have many advantages, including having a simple con-

* Corresponding author.
E-mail address: naoko.iwata@unipr.it (N. Iwata).

https://doi.org/10.1016/j.ijheatmasstransfer.2022.123203

Nomenclature

A	Amplitude of heat flux, W/m^2
a	Wavelet scale
c_p	Specific heat at constant pressure, J/kg/K
cvs	Coefficient of variation over space
cvt	Coefficient of variation over time
d	Diameter, m
E	Error
g	Gravity acceleration, m/s^2
H	Transfer function for the Gaussian filter
k	Thermal conductivity, W/m/K
M	Number of spatial steps
$mean$	Arithmetic mean
N	Number of time increments
p	Parameter related to frequency, Hz
Q	Heat load, W
q	Heat flux, W/m^2
R	Overall heat transfer coefficient, W/m^2/K
r	Radius, m
std	Standard deviation
T	Temperature, K
t	Time, s
U	Internal energy, J
u	Spatial coordinates in frequency domain
u_c	Cutt-off frequency
v	Time coordinates in frequency domain
W	Wavelet transform
y	Signal
z	Axial coordinate

Greek symbol

δ	Thickness, m
η	Non-dimensional time
ρ	Density, kg/m^3
σ_s	Surface tension, N/m
σ_d	Standard deviation, K
τ	Time, s
τ_{sh}	Time shift, s
ψ	Wavelet mother
ω_0	Non-dimensional frequency

Subscript

$crit$	Critical
ele	Electrical
env	Environment
$exact$	Known value
f	filtered
in	Inner
l	Liquid
out	Outer
$restored$	Calculated value
v	Vapor
w	Wall
z	Axial coordinate

struction, being lightweight and flexible, and having no internal wick structure. Low-cost and commercially available tubes can be used for PHPs without special processing. Consequently, the manufacturing costs of PHPs are lower than those of other two-phase thermal devices.

Until the early 2010s, most experimental studies used tubes or channels with a larger inner diameter of 1 mm or more [9,10]. However, some experimentations opened to the possibility of fabricating and employing PHPs with very thin channels or grooves of less than 1 mm [11–18]. Using micro-PHPs in heat exchangers allows the development of equipment that is lighter and more compact, and thus PHPs may be suitable for microelectronics. Despite the definition of micro device is well established for regular heat pipes [19], no clear definitions for micro-PHPs are provided, to the Authors knowledge, by the literature. However, previous studies [11–18] generally consider PHPs with an inner or hydraulic diameter lower than 0.7 mm as micro-PHPs.

Among other possible geometries, Si-based flat plate micro-PHPs have been actively investigated in the last decade due to the possibility of simpler set-ups manufacturing, suitable for direct fluid visualizations, i.e., having transparent substrates such as glass and polymeric material. The experimental effort has been mainly devoted to the study on the effects of influencing parameters, such as working fluid, filling ratio or inclination angle [11–18]. Qu et al. [11] investigated the characteristics of start-up, heat transfer, and flow characteristics of three Si-based micro-PHPs with different hydraulic diameters (0.251 mm, 0.352 mm, and 0.394 mm), changing working fluids (water, ethanol, R113, and FC-72), filling ratios, and inclination angles. Yang et al. [12] fabricated a 40 mm long Si-based PHP with identical rectangular microchannels 0.25 mm deep and of non-uniform width. The PHP operated at a heating power of 6 W or more with methanol as the working fluid. Yoon and Kim [13] conducted visualization experiments with a 5-turn Si-based micro-PHP and proposed a semi-analytic vapor-spring-liquid-mass model validated with experimental results. They also suggested that the vapor distribution in a micro-PHP affects its thermal performance [14]. Kim and Kim investigated the effect of the length and temperature of a micro-PHP condenser on thermal performance [15] and suitable working fluids, such as ethanol, FC-72, HFE-7000, R-245fa, and R-134a [16]. Lim and Kim proposed a novel channel layout of a Si-based micro-PHP for localized heating condition in which a heater covers only 2 % of the whole PHP surface [17]. Kamijima et al. [18] performed visualization experiment with a 11-turn Si-based micro-PHP and investigated the flow pattern with applying image-recognition technique to identify the flow characteristics and extract different flow patterns.

Although numbers of studies on Si-based flat plate micro-PHPs have been conducted, few studies have dealt with tubular micro-PHPs, despite the applicative advantages related to tubular layouts. In fact, tubular PHPs provide triaxial flexibility, whereas flat plate PHPs are flexible only biaxially, thus representing a suitable solution as a flexible thermal strap [20]. Moreover, Takawale et al. [21] reported that the tubular PHP performed better than the flat PHP due to the absence of lateral thermal conduction. On the other hand, tubular PHPs do not allow an easy employment of transparent inserts (e.g. glass or plastic tubes) for the direct fluid flow visualization, thus greatly increasing the complexity of a proper investigation on their thermal behavior.

Most of the experimentations on micro-PHPs have been mainly focused on either analysing the heat transfer rate averaged over the evaporator and condenser areas or evaluating the overall thermal resistance of the system. However, since the thermal behavior of micro-PHPs is inherently time-dependent and varies from turn to turn, investigating the local heat transfer is important to lead to a better understanding of the basic physical mechanisms underlying the micro-PHPs operation. In fact, the quantification of local heat transfer in PHPs provides important pieces of information not only in terms of fluid oscillations, but also in terms of phase-change phenomena. Mameli et al. [22] estimated the local heat transfer coefficient by measuring both tube wall and internal fluid temperatures in the evaporator section of a two-turns PHP. They reported a minimum heat flux for the stable fluid motion and a critical heat flux before the final dry-out. Nevertheless, in micro-PHPs a direct measurement of the fluid temperature can be hardly achieved due to the very limited geometry that hin-

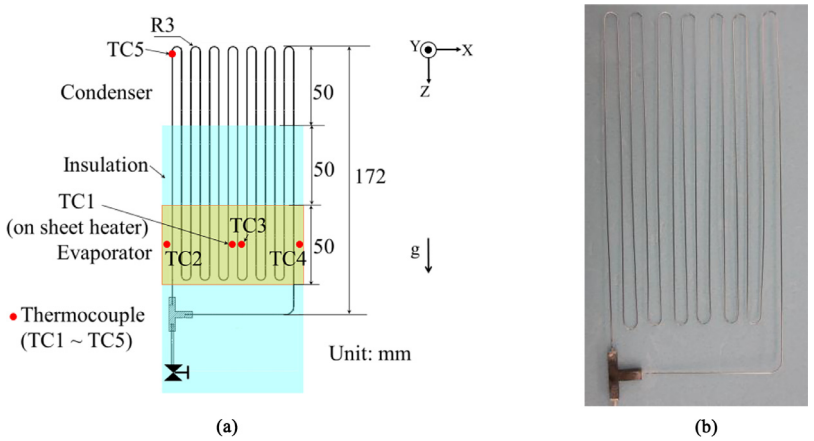

Fig. 1. (a) Schematic and (b) appearance of micro-PHP.

ders the installation of temperature sensors in the flow path. Jo et al. [23] measured the distributions of temperature and heat flux at the fluid-wall interface of the Si-based micro-PHP which has a multilayer structure in the inner wall. Since silicon is largely transparent to infrared (IR) radiation, the temperature of the inner and outer walls of the multilayer coated with a thin, IR opaque film can be measured by an IR camera [24].

Recently, Cattani et al. [25] proposed a non-intrusive local heat flux estimation procedure based on thermographic measurements on the external wall of a single-loop PHP, used as inputs for the Inverse Heat Conduction Problem (IHCP) resolution approach. Since the adoption of a transparent sapphire insert allowed simultaneous wall and fluid temperature measurements, the heat fluxes estimated were proven to be correlated to different flow regimes occurring in PHPs. Pagliarini et al. [26] adopted a similar wall-to-fluid heat flux estimation procedure within the adiabatic section of a multi-turn PHP fully made of aluminium under micro-gravity condition. The results, additionally processed by a statistical approach, verified the capability of the inverse method to provide a similar description of the device working regimes and oscillation frequencies to that obtained by other techniques, e.g. employment of pressure transducers or evaporator/condenser temperature monitoring.

In order to understand the thermo-fluid interactions occurring in the condenser section of tubular micro-PHPs, this study proposes to extend the method, presented in [26], which is suitable for opaque pipes, i.e., when the fluid is not directly visible. Thermographic acquisitions are used as inputs for the IHCP resolution approach. The resulting space-time heat flux maps are therefore statistically reduced to quantitatively information identifying the device working regimes at varying heat loads to the evaporator. In addition, a frequency analysis based on the Wavelet method is carried out to obtain a channel-wise description of the fluid oscillatory behavior in the overall device. The provided data are believed to be useful for the understanding of micro-PHPs thermal behavior, as well as for the improvement of existing numerical models.

2. Experimental setup

A stainless-steel (SUS304) tube with inner and outer diameters of 0.32 mm and 0.52 mm, respectively, was bent into 7 turns as shown in Fig. 1. The stainless-steel capillary tubes were used due to their commercial availability and cost-effectiveness: in this way the implemented device is representative of a possible industrial application. HFC-134a was charged as a working fluid. In the temperature range from 280 K to 350 K, the inner diameter is less than the critical maximum diameter d_{crit} defined by the following equation [27]:

$$d_{crit} = 2\left[\frac{\sigma_s}{g(\rho_l - \rho_v)}\right]^{1/2} \quad (1)$$

where σ_s, g, ρ_l, and ρ_v are the surface tension, gravitational acceleration (9.81 m/s^2), liquid density, and vapor density, respectively. Using the properties of NIST Reference Fluid Thermodynamic and Transport Properties Database mini-REFPROOP version 10.0 [28], d_{crit} for HFC-134a at 280 K to 350 K are calculated to be 1.8 mm and 0.99 mm, respectively. Before charging the working fluid, the airtightness of the micro PHP was checked with gas nitrogen up to 2 MPaG. Assuming that the inside of the PHP is filled with the saturated two-phase working fluid when the PHP is operating, the internal pressure of 2 MPaG corresponds to the saturation pressure of HFC-134a at 70 °C [28]. The experiments were conducted as long as the evaporator temperature did not reach 70 °C.

Fig. 2 shows the experimental setup. The evaporator channels were attached to a 3 mm-thick spreader by aluminium tapes, while the heat load was provided by a polyimide sheet heater, placed on the back of the spreader. The condenser tubes were coated with a thin film of high-emissivity paint. The evaporator and adiabatic section were insulated, while the condenser was cooled down by natural convection of air. The condenser temperature was monitored by an infrared camera (FLIR SC7000, space resolution: 640 × 512 pixels accuracy: ±1 K, thermal sensitivity at 303 K: 20 mK). For the present configuration, the infrared spatial resolution at target surface was equal to 0.156 mm/pixel. During the tests, the PHP operated in vertical bottom heat mode, i.e. with the evaporator at the bottom. As shown in Fig. 1(a), in the coordinate system of this study, the direction of gravity (i.e., the longitudinal direction of the PHP from the top of the condenser to the evaporator) was considered as +z direction.

Five type-T thermocouples were attached: one was on the sheet heater, three were on the metal plate of the evaporator, and the other was on the condenser. The last was to control the correspondence of the measured values between the camera and thermocouple. A stepwise heat load was provided to the evaporator from 0.1 W to 5 W (until the operating limit) by a DC power supply (HEWLETT PACKARD 6631B). The experimental data were collected by a data acquisition system (AGILENT 34970A), for each power input, when the device reached the pseudo-steady state. The acquisition frequency of the camera and the thermocouples were 18 Hz and 1 Hz, respectively. The more details of the experimental setup were given in the authors' previous study [29]. The measurement uncertainties of the T-type thermocouple and the voltage and the current of the power supply were ± 0.2 °C, ± (0.03%

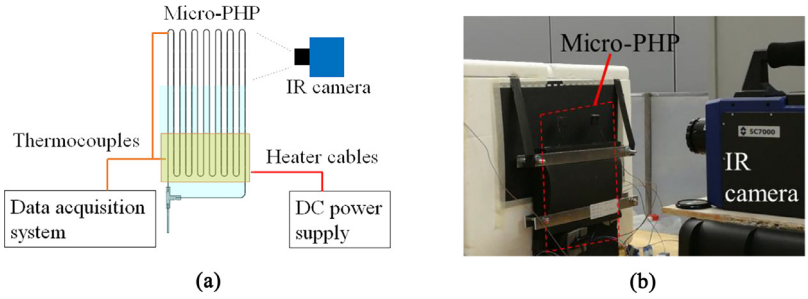

Fig. 2. (a) Schematic and (b) appearance of test setup.

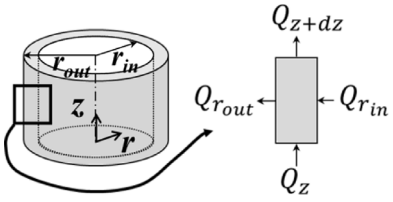

Fig. 3. Energy balance at the infinitesimal wall section.

full scale + 2 mV), and ± (0.2 % full scale + 1 mA), respectively. The full scale of the voltage and the current of the power supply were 8 V and 10 A, respectively. The measurement uncertainty of the data acquisition system for the temperature measurement was 1.0 °C.

3. Heat flux estimation

3.1. Estimation procedure

Using the time-space temperature maps acquired by the IR camera as input data, the local wall-to-fluid heat flux was evaluated by solving the IHCP in the tube wall. Specifically, each straight part of the PHP channels belonging to the condenser section was modelled as a 2D-axisimmetric solid domain, outlined in Fig. 3. By assuming the thin-wall approximation, the temperature on the external surface was considered equal to that on the internal surface. This thin-wall-approximation was verified for all the experimental tests. In addition, due to experimental observations, the temperature gradients along the tube circumference were considered to be negligible.

Following the previous assumptions, the local energy balance equation becomes:

$$\frac{dU}{dt} = Q_z - Q_{z+\Delta z} + Q_{r_{in}} - Q_{r_{out}} \tag{2}$$

where Q_z and $Q_{z+\Delta z}$ are the conductive terms related to the axial direction z, while $Q_{r_{in}}$ and $Q_{r_{out}}$ are the heat exchange amount between the inner tube wall and the fluid and the power dissipated to the environment by natural convection, respectively. The time derivative of internal energy is presented as $\frac{dU}{dt}$. Each energy term of Eq. (2) is expressed as:

$$\frac{dU}{dt} = \rho_w c_{pw} \frac{\partial T}{\partial t} \cdot \pi \left(r_{out}^2 - r_{in}^2\right) \cdot \Delta z \tag{3a}$$

$$Q_z = -k_w \frac{\partial T}{\partial z} \cdot \pi \left(r_{out}^2 - r_{in}^2\right) \tag{3b}$$

$$Q_{z+\Delta z} = -k_w \frac{\partial T}{\partial z} \cdot \pi \left(r_{out}^2 - r_{in}^2\right) - k_w \frac{\partial^2 T}{\partial z^2} \cdot \pi \left(r_{out}^2 - r_{in}^2\right) \cdot \Delta z \tag{3c}$$

$$Q_{r_{in}} = q \cdot 2\pi r_{in} \cdot \Delta z \tag{3d}$$

$$Q_{r_{out}} = \frac{(T - T_{env})}{R_{env}} 2\pi r_{out} \cdot \Delta z \tag{3e}$$

where ρ_w, $c_{pw}$and k_w are the density (kg/ m^3), specific heat (J /kg/K), and thermal conductivity (W/m/K) of the tube wall, respectively. The outer and inner radiuses of the tube are represented as r_{out} and r_{in} as shown in Fig. 3. In Eq. (3e), T, T_{env}, and R_{env} are the fluid temperature, the environmental temperature, and overall heat transfer coefficient between the tube outer wall and the surrounding environment, respectively. For T_{env}, 26°C was adopted based on the measured environment temperature during the experiments; R_{env} was taken equal to 10 W/m^2/K, and it was measured by a preliminary test using an electrically heated sample tube. By substituting equations (3a) - (3e) into Eq. (2), the heat flux from the fluid to the tube inner wall q is found as follows:

$$q = \frac{(\rho_w c_{pw} \frac{\partial T}{\partial t} - k_w \frac{\partial T^2}{\partial z^2}) \cdot \left(r_{out}^2 - r_{in}^2\right) + \frac{(T - T_{env})}{R_{env}} \cdot 2r_{out}}{2r_{in}} \tag{4}$$

Eq. (4) was solved by means of the finite difference method as follows.

$$q(z,t) = \frac{\left(\rho_w c_{pw} \frac{T_{(z,t+\Delta t)} - T_{(z,\Delta t)}}{\Delta t} - k_w \frac{T_{(z+\Delta z,t)} + T_{(z-\Delta z,t)} - 2T_{(z,t)}}{(\Delta z)^2}\right) \cdot \left(r_{out}^2 - r_{in}^2\right) + \frac{(T_{(z,t)} - T_{env})}{R_{env}} \cdot 2r_{out}}{2r_{in}} \tag{5}$$

Due to the noise level of the raw data, a regularization method was applied to the temperature distributions to reliably solve it. The fluid-to-wall heat flux can be obtained by adopting in Eq. (5) the filtered temperature T_f instead of the measured temperature T. As highlighted in the flowchart in Fig. 4, filtering was carried out in the following way: first, discrete Fourie transform was performed on the temperature map data acquired by the IR camera, which consists of M spatial steps Δz and N time increments Δt, i.e., $M \times N$ elements. The discrete Fourier transform of the measured $M \times N$ temperature distribution T results in:

$$\mathcal{F}(T) = \tilde{T}(u,v) = \sum_{g=0}^{M-1} \sum_{h=0}^{N-1} T(g,h) e^{-j2\pi \frac{u}{M} g} e^{-j2\pi \frac{v}{N} h} \tag{6}$$

where u and v are the spatial and time coordinates in the frequency domain, respectively. Second, the Gaussian filter was adopted to the discrete Fourier transform:

$$\mathcal{F}\left(T_f\right) = \tilde{T}_f(u,v) = H(u,v) \cdot \tilde{T}(u,v) \tag{7}$$

where $H(u,v)$ is the transfer function for the Gaussian filter. It is defined as:

$$H(u,v) = e^{-\left(u^2+v^2\right)/2u_c^2} \tag{8}$$

where u_c is the cut-off frequency. Last, the Fourier image is converted back to the time-space domain:

$$\mathcal{F}^{-1}\left(\tilde{T}_f\right) = T_f(m,n) = \frac{1}{M \cdot N} \sum_{k=0}^{M-1} \sum_{l=0}^{N-1} \tilde{T}_f(k,l) e^{j2\pi \frac{k}{M} m} e^{j2\pi \frac{l}{N} n} \tag{9}$$

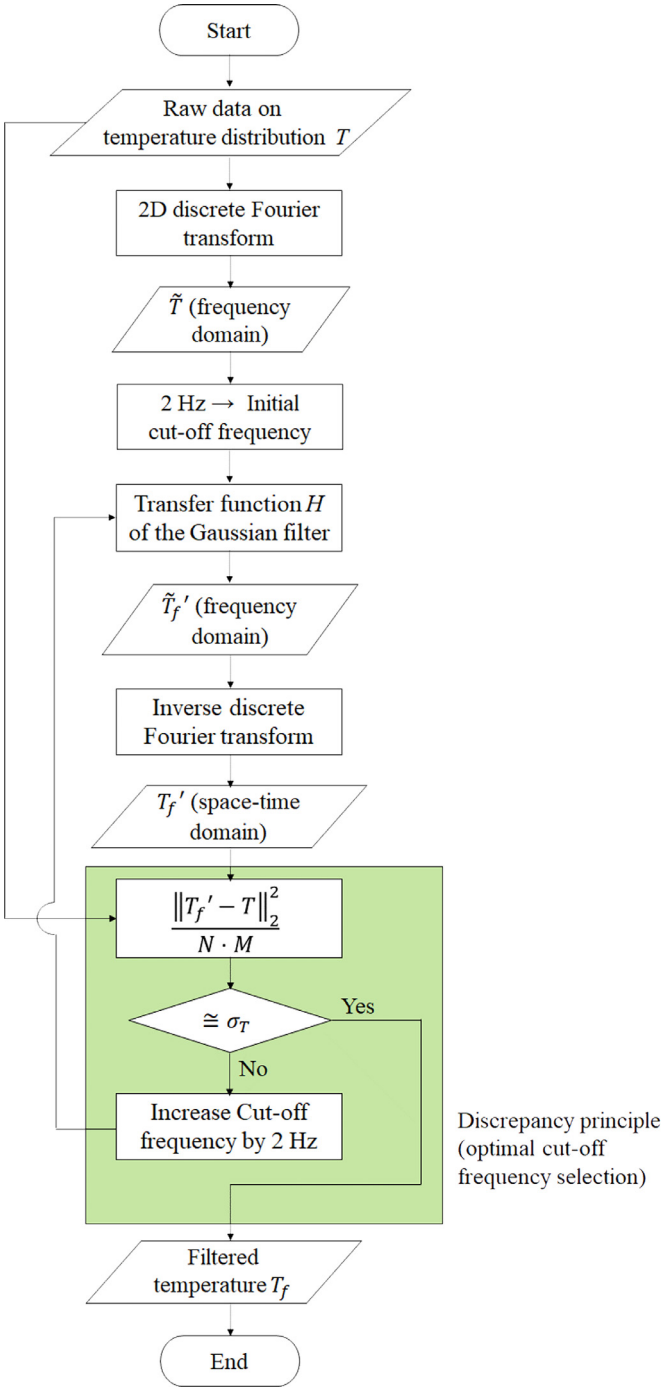

Fig. 4. Flowchart of filtering procedure.

In practice, the optimum cut-off frequency is unknown a priori. In this study, it was obtained by an iterative calculation where the initial cut-off frequency was set at 2 Hz and increased by 2 Hz until the optimum frequency was found, as shown in Fig. 4. According to the discrepancy principle [30], when the difference between the measured T and the filtered T_f temperatures are nearly equivalent to the standard deviation of the raw measurements, the solution to the inverse problem is considered sufficiently accurate. The cut-off frequency was defined as the frequency satisfying the following conditions:

$$\frac{\left|\left|T_f - T\right|\right|_2}{\sqrt{N \cdot M}} \cong \sigma_d \tag{10}$$

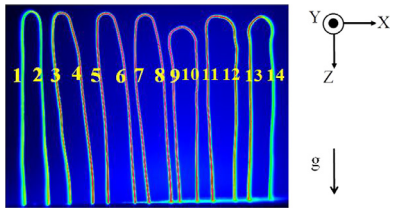

Fig. 5. Channel identification.

where $||\ \ ||_2$ stands for the 2-norm, $N \cdot M$ is the size of the matrix T and σ_d is the standard deviation of the raw data, estimated by measuring the wall temperature distribution while maintaining the system under isothermal conditions.

The processing target area of the condenser is constituted by every straight tube where the distance from the U-shaped apex is from 12 mm to 45 m, which is equivalent to 214 pixels in the longitudinal direction of the IR camera. Each tube is identified from ch 1 to ch 14 as shown in Fig. 5.

3.2. Validation

The post-processing method presented in the previous section was validated to assess its reliability for the present application. Synthetic temperature data were first generated by solving the direct problem within a COMSOL Multiphysics® environment. Here, a known distribution of the heat flux $q_{exact}(z,\ t)$ was provided as boundary condition at the internal wall surface of the test section of Fig. 3, simulating the heat transfer by forced convection occurring inside a single PHP branch in transient conditions. According to the expected results in the real cases, the convective heat flux q_{exact} was assumed as a sinusoidal function characterized by time-space variations, where L_z is the length of the considered channel portion:

$$q_{exact}(z,t) = A \cdot \cos(p\pi t) + 125 - \frac{z \cdot 250}{L_z} \tag{11}$$

The noisy temperature distributions were therefore used as inputs for the IHCP solution approach, i.e., for Eq. (5). The effectiveness of the proposed approach at different heat flux amplitudes and frequencies was evaluated by taking A equal to 2000 and 5000 W/m^2, while the p parameter was varied from 1 to 2, corresponding to frequencies of 0.5 and 1 Hz, respectively. According to the literature [31], the chosen values of amplitude and frequency are representative of the oscillatory phenomena that characterize the PHPs thermo-fluid dynamics within the adiabatic section.

The resulting temperature distributions were then spoiled by a Gaussian noise level, characterized by a standard deviation σ_d equal to 0.06 K. Specifically, such a value was considered since it represents the noise level related to the adopted experimental set-up, quantified by means of isothermal measurements on the device. The thin-wall approximation adopted in the Section 3.1 was furthermore validated by the application of Fourier's law to the tube wall. The heat conduction in the tube wall is expressed by the Fourier's law as follows.

$$q = -k_w \frac{dT}{dx} \tag{12}$$

Eq. (12) was expressed by finite differences and the temperature difference in the wall between the inner and outer surfaces of the tube was calculated as follow:

$$\Delta T = -\frac{\delta_w q}{k_w} \tag{13}$$

where δ_w is wall thickness and q is the convective heat flux exchange between the fluid and the wall. For a maximum heat flux

Table 1
estimation error E_q for different amplitudes and frequencies of q_{exact} (considered noise level $\sigma_d = 0.06$ K).

Amplitude [W/m^2]	Frequency [Hz]	Error [%]
2000	0.5	10
2000	1	16.1
4000	0.5	7.4
4000	1	14.2

equal to 6000 W/m^2, with a wall thickness of 0.1 mm and considering the thermal conductivity of SUS304, 15 W/m^2/K [32], the maximum temperature difference between the inner and outer surfaces of the tube is about 0.03 K. This is half of the noise level related to the experimental set-up (0.06 K). However, it must be pointed out that the adopted inverse approach in transient conditions might be affected by the thermal inertia of stainless-steel walls that eventually hamper a clear observation by thermography of high-frequency phenomena, e.g., alternation of slugs and plugs within the fluid flow [26]. To study such inertial effects on the wall-to-fluid heat flux evaluation procedure, the direct problem was solved by adopting distributions of q_{exact} with p ranging from 2.5 to 8 and A equal to 2000 W/m^2. For oscillation frequencies greater than 4 Hz, the maximum variation of the external wall temperature was found to be lower than the noise level of the experimental set-up, suggesting that the thermographic measurements on the outer wall can catch transient phenomena that occur in a time higher than 0.25 s. Other significantly faster phenomena cannot be fully perceived due to the filtering effect of the stainless-steel wall.

To quantify the efficiency of the applied approach at different signal-to-noise levels, an error analysis was performed by evaluating the estimation error E_q, defined as follows:

$$E_q = \frac{||q_{restored} - q_{exact}||_2}{A\sqrt{M \cdot N}} \tag{14}$$

where $q_{restored}$ is the wall-to-fluid heat flux distribution evaluated by means of Eq. (5).

Since the added noise intrinsically depends on the random sequence generated, the error estimation procedure was replicated for 100 different random sequences of noise added to the synthetic temperature distributions and an average value of E_q was calculated for each validation case.

In Table 1, values of E_q are listed for all the considered amplitudes and oscillation frequencies of q_{exact}. Here, the estimation error increases with frequency, while it decreases with the increase of A, in accordance with the validation outcomes presented by Pagliarini et al. [26] for different PHP material and geometry. The maximum estimation error within the analyzed application ranges was found to be equal to 16.1 % of q_{exact}, thus providing a reference for the accuracy of the proposed inverse approach.

4. Results and discussion

4.1. Flow regime

The fluid oscillation started at the minimum electrical power input (Q_{ele}), 0.1 W. The oscillation is intermittent with up to five seconds of stopover in the whole PHP and the liquid slug or the vapor plug from the evaporator did not reach the top of the condenser. The oscillation amplitude increased along with the increase of the heat input. At the power input of 0.5W, it was observed that the slug/plug from the evaporator penetrate the condenser and moved to the next tube repeatedly. Fig. 6 shows the representative IR images of the condenser at power input of 0.1 W and 0.5 W. The images were extracted every three seconds from a nine-seconds video taken during pseudo-steady state. In addition, the videos S1 and S2, taken by the IR camera during pseudo-steady states at the power input of 0.1 W and 0.5 W, respectively, are given as the supplementary data. The images and videos show that the flow in higher temperature than the surrounding rises up from the bottom (the adiabatic and evaporator sides) to the condenser in both power input cases. The interface between the higher and lower temperature sections, shown as a representative pink arrow in Fig. 6, is considered to be a meniscus of vapor and liquid. The higher temperature part consists of a liquid slug or a chain of slugs/plugs heated in the evaporator. The fluid coming from the evaporator stops in the middle of the condenser and does not return to the evaporator at 0.1 W. It was caused by the low driving force that did not overcome the counterforce of the gravity or the pressure loss and the rapid temperature drop of the liquid slugs due to the heat exchange with the tube wall of the condenser. When the heat input was increased, the driving force of the fluid oscillation increased, which led the higher amplitude of the oscillation and thus the overall penetration of the plug/slug in the condenser and more persistent and active oscillation. However, even at 0.5 W, the flow was still intermittent in all the tubes: the fluid flow n from the evaporator to the condenser rose up to the bending part at once and then stopped for less than a few seconds. It started flowing again in the same or the other directions. This intermittent oscillation was due to insufficient heat input for the continuous active oscillation.

Fig. 7 shows the time variation of wall surface temperature distribution of the tube positioned in the center of the PHP (ch9) at power input of 0.1 W and 0.5 W. The temperature shown was filtered by the method described in Section 3.1. The position of ch9 is shown in Fig. 5. The duration time that the flow stopped (i.e., stopover period) at 0.1 W was more than 5 s larger than that of 0.5 W. As shown in Fig. 5, the flow from the evaporator stopped at the middle of the tube at 0.1 W whereas the fluid flowed more actively at power input of 0.5 W.

Along with increasing the power input, the oscillation became more continuous and active. The stopover period more than one second was no longer appeared. From 1.5 W to 3.5 W, the fluid direction changed with time and tubes. Figs. 8 and 9 show the representative IR images of the condenser at power input of 2.5 W and 4.5 W, respectively. Moreover, the IR videos S3 and S4 during pseudo-steady state with the power inputs of 2.5 W and 4.5 W, respectively, are also given as the supplementary data. The images were extracted every 0.5 s from the video taken during pseudo-steady state. In Fig. 8, the upper four images (Figs. 8 (a)) show the whole PHP and the lower images (Figs. 8 (b)) are the central three tubes (i.e., 6 channels from ch5 to ch10) extracted from the top image because they were hardly distinguishable in the upper images due to the wide temperature scale. In both power input cases the temperature of edge tubes was more than 5 °C lower than that of the central tubes. In Fig. 8, the flow directions shown as the yellow arrows varied depending on the time and channels. The flow from the evaporator tended to pass through the condenser and reach the evaporator in the next tube, but it did not flow in one direction in all tubes, it was relatively random.

This random flow was also observed from the temperature distribution of the channels. Fig. 10 shows the temperature history for 1 minute at an input power of 2.5 W for the position of z=40 mm in the central six tubes (i.e., three turns), indicated by yellow dots and numbers in Fig. 8(b). The temperature shown was not filtered, but measured raw data. Different trend was shown between left two turns (ch5–6 and 7–8) and right one turn (ch9–10). In the latter turn, the ch9 temperature was always 1 °C higher than that of ch10, even though both temperatures fluctuated with the amplitude of 0.5 °C at the maximum. Considering that the condenser wall temperature decreases along the fluid flow from the evaporator due to the heat exchange with surroundings, the fluid flowed

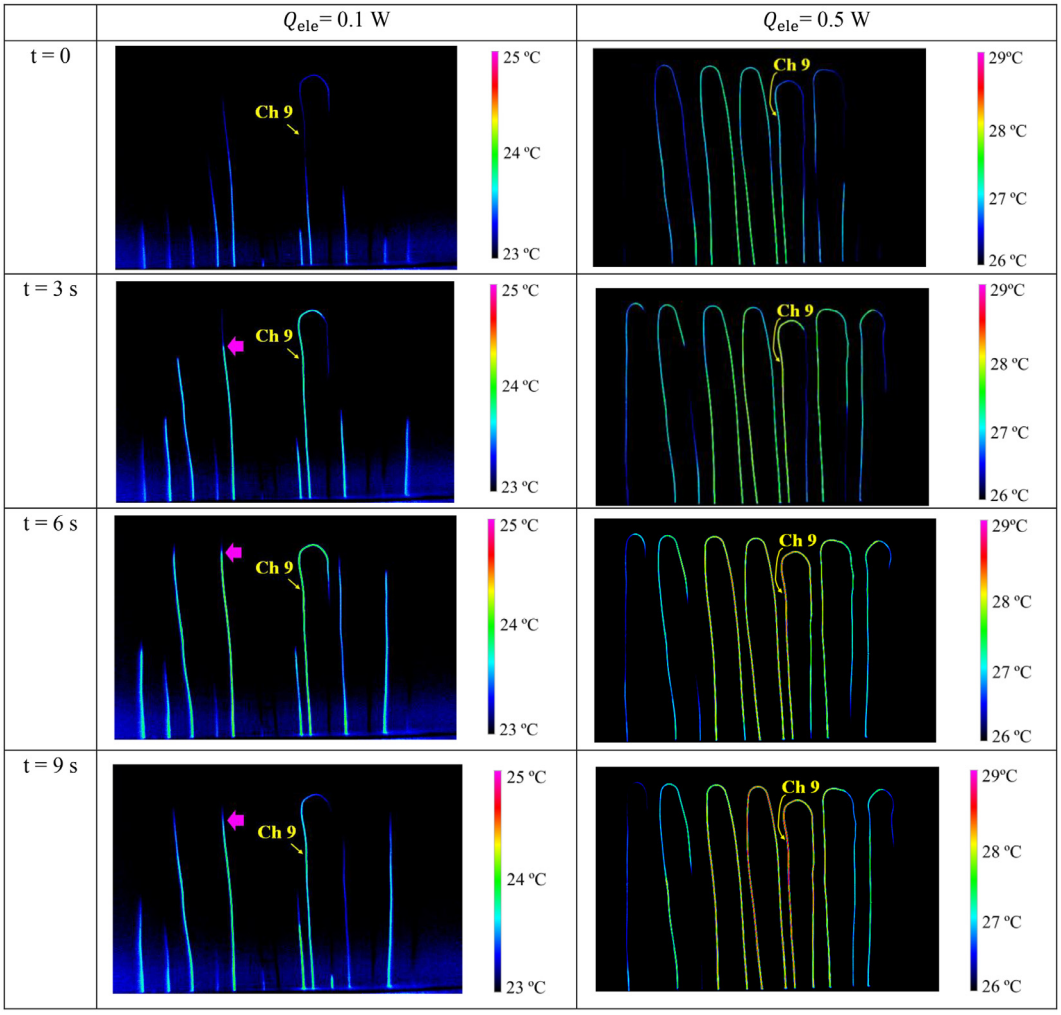

Fig. 6. IR images at 0.1 W and 0.5 W for nine seconds. The time shown are relative, not absolute.

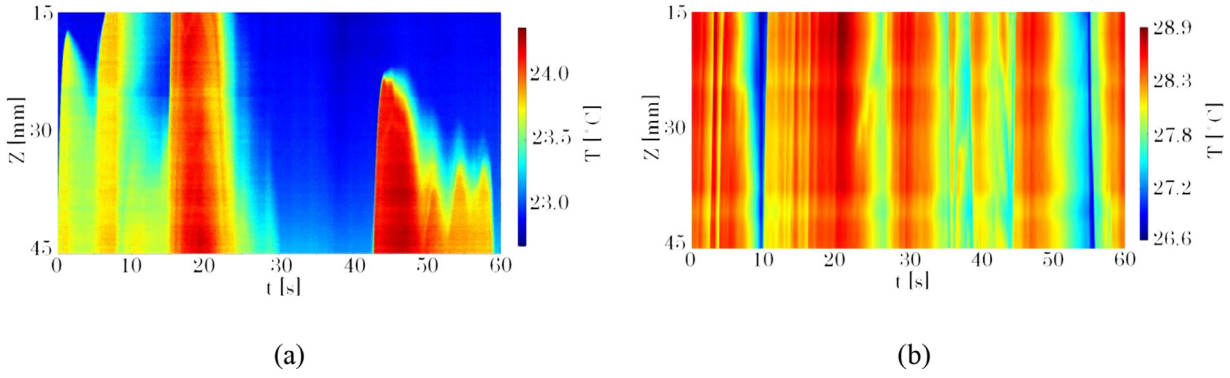

Fig. 7. Wall temperature distribution of ch9 at power input of (a) 0.1 W and (b) 0.5 W.

from left to right (from ch9 to ch10 or -x to +x) with local oscillating. On the other hand, in the two left turns, the temperature of the even-numbered tubes was basically higher than that of the odd-numbered tubes, but periodically the temperatures of both were equal or the temperature of the even-numbered tubes were lower than that of the odd-numbered tubes. It indicated that in these two turns basically the fluid flowed from right to left (+x to -x) but the direction varied depending on time.

At power input of 4 W or more, in all seven-turns, the fluid flowed from the even-numbered tube to odd-numbered tube (from right to left or from +x to -x), as the yellow arrows in Fig. 9. In every turn, the temperature gradually decreased from the bottom of the even-numbered tube to the bottom of the odd-numbered tube. It indicated that the hot fluid from the evaporator moved from the right to left through the condenser with dissipating the heat to the environment and reducing the temperature.

Fig. 11 shows the temperature history for 1 minute at an input power of 4.5 W for the position of z=40 mm in the central six tubes (i.e., three turns), indicated by yellow dots and numbers in Fig. 8(b) and 9. Same as Fig. 10, the temperature shown

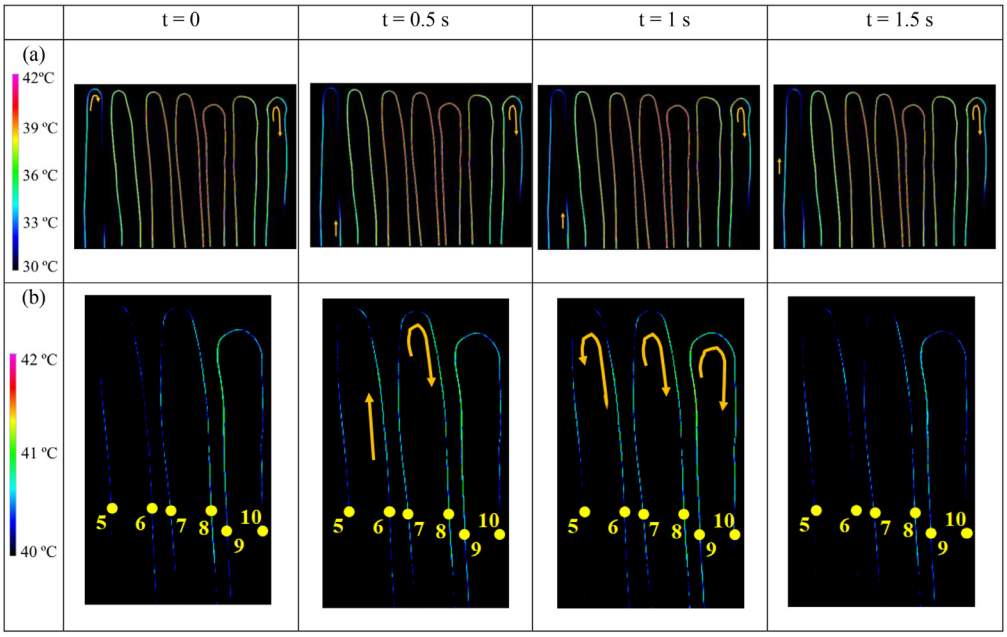

Fig. 8. IR images at 2.5 W for 1.5 s: (a) all tubes and (b) extracted tubes (ch5 – 10). The time shown are relative, not absolute (The same applied to Fig. 9).

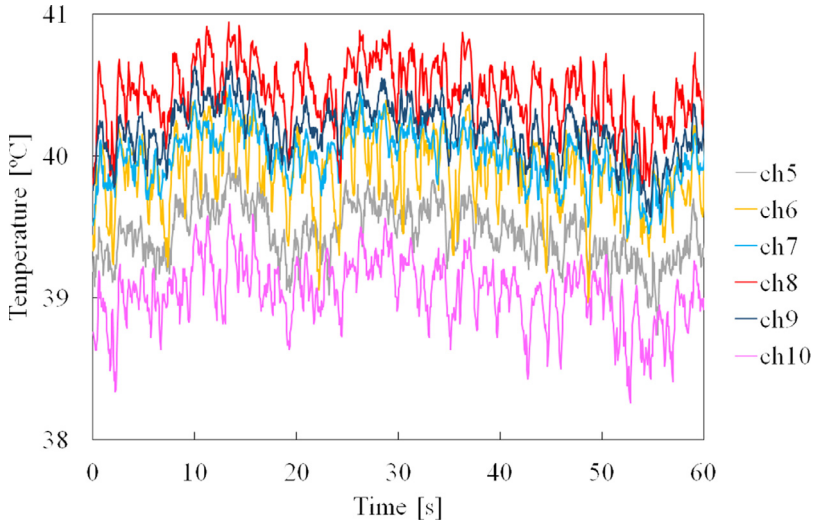

Fig. 9. IR images at 4.5 W for 1 s.

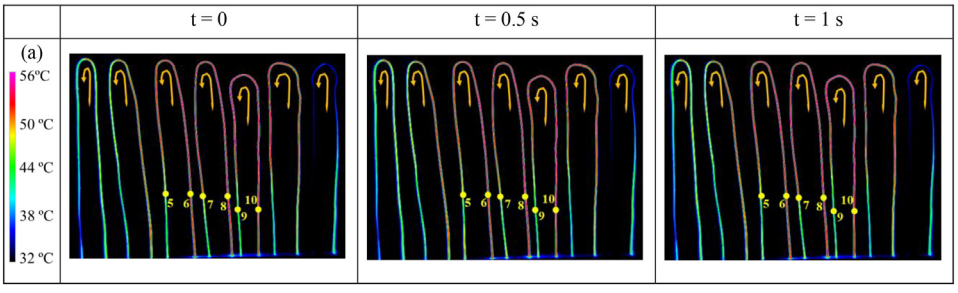

Fig. 10. Temperature histories of ch5-8 at z = 40 mm for one minute with 2.5 W power input.

was not filtered but measured raw data. Contrary to Fig. 10, the temperatures of even-numbered tubes (i.e., ch6, 8, and 10) kept more than 2 °C higher than the odd-numbered tubes (i.e., ch5, 7, and 9). This is resulted from the hot fluid flowing from the bottom of odd-numbered tubes (i.e., the evaporator) to the adjacent even-numbered tube with lowering its temperature by dissipating heat to the environment. Due to the fact that the fluid flowed in the same direction in all turns, there was a possibility of the circulation flow in the PHP. Kim and Kim [16] reported that the flow pattern of the 10-turn micro-PHP with HFC-134a charged at 50% filling ratio changes from the pulsating flow to the circulation flow along with the heat input increments in the condenser

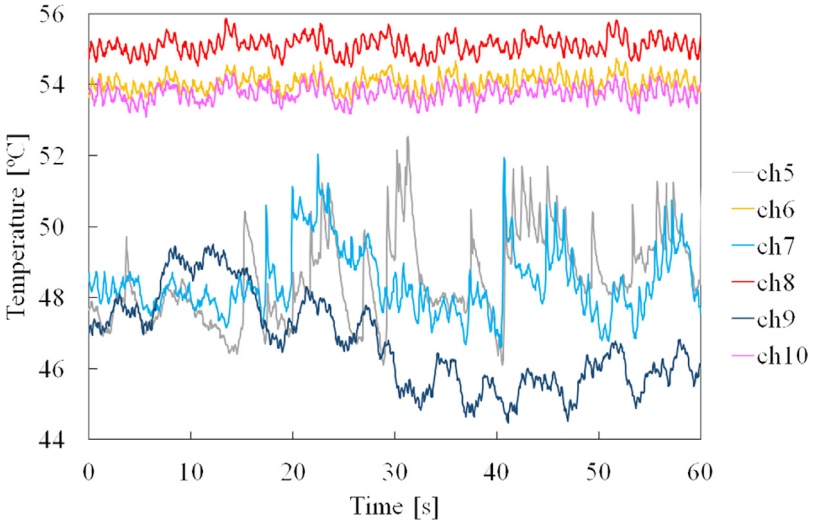

Fig. 11. Temperature histories of ch5-8 at z = 40 mm for one minute with 4.5 W power input.

temperature range of 20 °C to 40 °C. The PHP in this study has some disadvantages that make it difficult to maintain the circulation flow compared to theirs, such as longer adiabatic section and smaller number of turns. Moreover, since not the whole PHP but only the condenser was visualized by the IR camera, it cannot be concluded with 100% assurance that the fluid was circulating in the PHP. In Fig. 11, compared to the temperature stability of the even-numbered tubes with the oscillation amplitude of less than 2 °C, the temperature of the odd-numbered tubes fluctuated more, with a maximum of 6 °C. It is possibly caused by the local oscillation of the fluid or the non-uniformity of the heat exchange between the fluid and the environment including phase-change.

4.2. Wall temperature and heat flux

Fig. 12 shows the one-minute history of the wall temperature and the corresponding heat flux calculated by the IHCP at four tubes positioned near the edges (ch1 and 2) and the center (ch7 and 8), at the power input of 0.5 W, 2.5 W, and 4.5 W. Same as Fig. 7, the temperature shown was filtered by the method described in Section 3.1. The period extracted was after reaching pseudo-steady state, at each heat input condition. A clear difference of flow regimes was shown between low heat input and high input.

At heat input of 0.5W, the flow was intermittent in all tubes as shown in the previous section. In the edge tubes, the fluid coming from the evaporator flowed from ch1 to ch2 and it seldom flowed down to the adiabatic section of ch2. On the contrary, in the middle tubes the fluid often flowed from one tube to the other tube in both directions with penetrating the tube in the condenser.

Almost the same behavior was observed at higher heat input values. At 2.5 W, the fluid rose up from the evaporator of ch2 and the vapor/liquid meniscus of the working fluid that is shown as the interface of high and low temperatures oscillated in the condenser section of ch2. It was due to the fact that the oscillation was not fully penetrated overall condenser sections of the ch2. On the other hand, the fluid oscillated and reached overall condensers more actively in the middle tubes. This kept the condenser wall temperature of ch7 and 8.5–10 ℃ higher than that of ch2. The oscillation frequency and the amplitude of the heat flux was increased along with the increments of the heat input regardless the tube position.

At the power input of 4.5 W, the flow became in one direction from the even-numbered channel to odd-numbered channel (from right to left) and a meniscus oscillated in the condenser at each turn, as the IR video S4 and images of Figs. 9 and 11 shows. This behavior reflected in the wave-like oscillation of the heat flux shown in Fig. 12(c).

The heat flux in each power input showed the positive values because the condenser was cooled by natural convection and therefore the condenser temperature could not be lower than the ambient temperature.

4.3. Coefficient of variation

The inverse heat transfer approach provides a large amount of data about local time-space heat fluxes exchanged at the wall-fluid interface that needs to be adequately reduced to be efficaciously employed. To precisely quantify the thermal behavior of the PHP in terms of time and space distribution of the wall-to-fluid heat flux in every channel, two coefficients were introduced by Pagliarini et al. [26]: the coefficient of variation over time (cvt) and along space (cvs), respectively. For the heat flux at position z_i of the n-th tube, the cvt_{n,z_i} from time τ_1 to τ_M is expressed as follows:

$$cvt_{n,z_i} = \frac{std(|q_n(z = z_i, \quad \tau = \tau_1, \ldots, \tau_M)|)}{mean(|q_n(z = z_i, \quad \tau = \tau_1, \ldots, \tau_M)|)} \tag{15}$$

where *std* and *mean* refer to the standard deviation and the arithmetic mean, respectively. For the heat flux of the *n*-th tube at time τ_j, the cvs_{n,τ_j} from position z_1 to z_N in the Z-direction is expressed as follows.

$$cvs_{n,\tau_j} = \frac{std\left(\left|q_n\left(z = z_1, \ldots, z_N, \ \tau = \tau_j\right)\right|\right)}{mean\left(\left|q_n\left(z = z_1, \ldots, z_N, \ \tau = \tau_j\right)\right|\right)} \tag{16}$$

In the present study, *cvt* and *cvs* were evaluated for a 30-mm section of all condenser tubes during sixty seconds of pseudo-steady state at each heat input condition.

Fig. 13 shows *cvt* and *cvs* for three different power input conditions of 0.5 W, 2.5 W, and 4.5 W.

At low heat input of 0.5 W, the *cvt* was as high as 1 to over 2 in each tube and it decreases along with increasing of power input. The *cvs* showed the high peaks over 2 at power inputs of 0.5 W and 2.5 W, whereas they weakened to less than 1.5 at 4.5 W. This results of *cvs* showed the difference in flow regimes between low and high-power inputs described in the previous section, i.e., flow in random direction (0.5 W and 2.5 W) and unidirectional flow in whole PHP (4.5 W).

At low heat input, the variations of the heat flux over time and along the axial coordinate were significant, which caused by

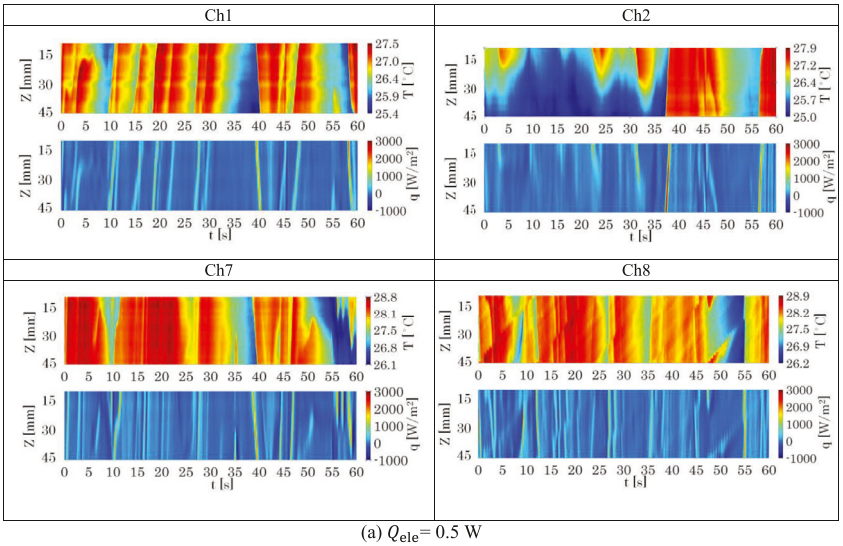

(a) Q_{ele}= 0.5 W

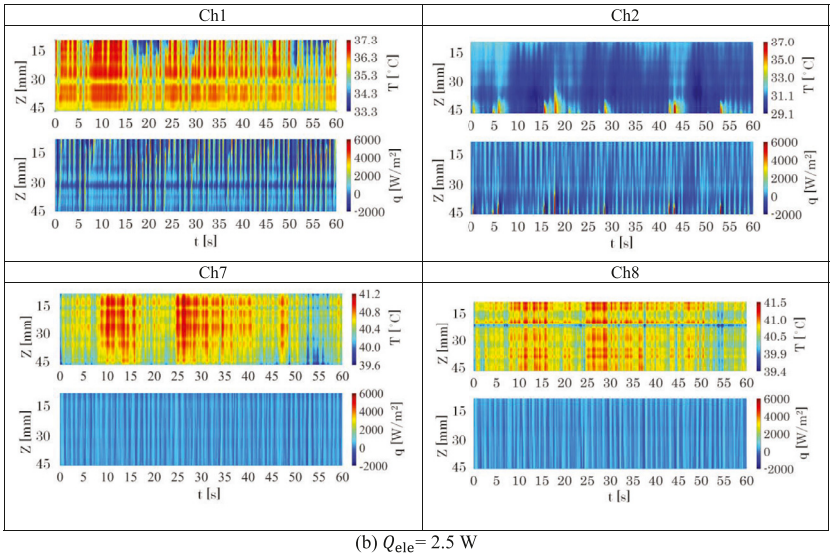

(b) Q_{ele}= 2.5 W

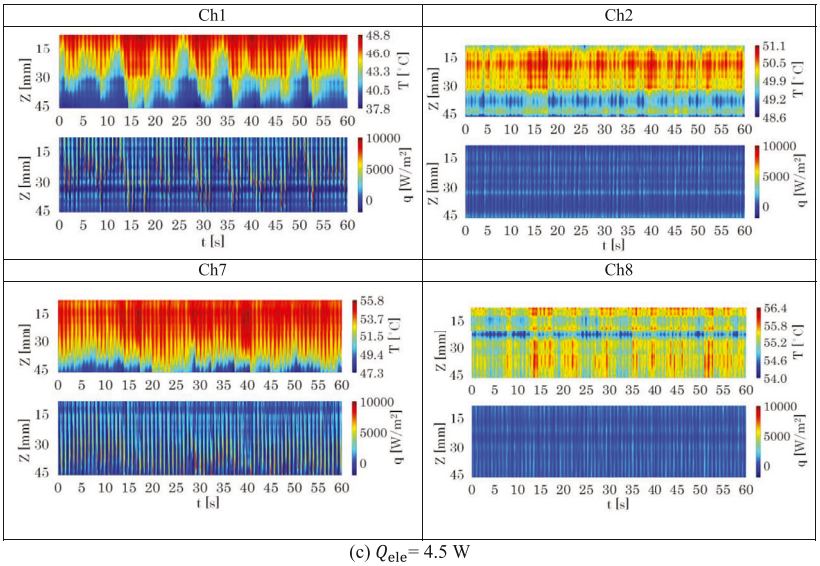

(c) Q_{ele}= 4.5 W

Fig. 12. Wall temperature distribution and heat fluxes of channel 1, 2,7, and 8 at power input (a) 0.5W, (b) 2.5W, and (c) 4.5W. The vertical axes indicate the distance from the top of the condenser.

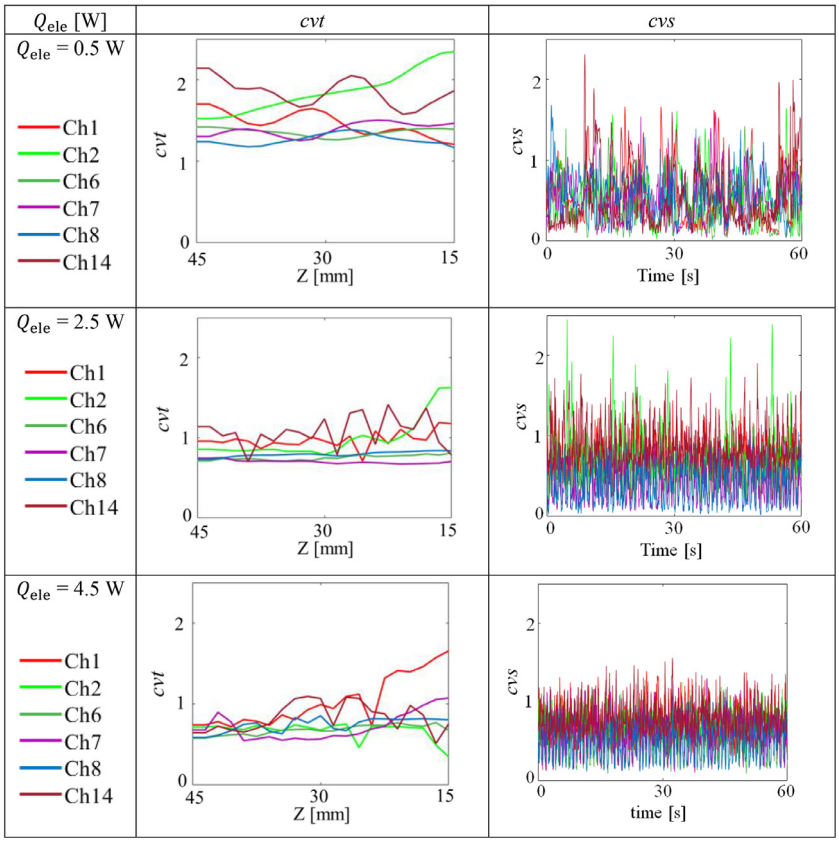

Fig. 13. *Cvt* and *cvs* of estimated heat flux at 0.5 W, 2,5 W, and 4.5 W.

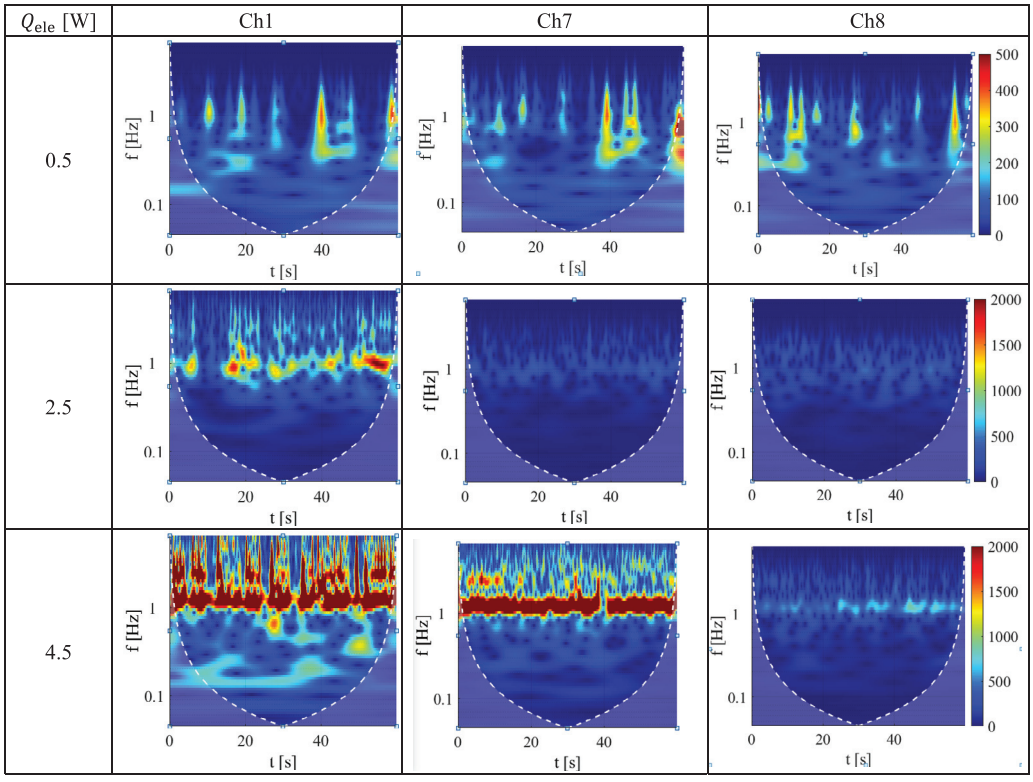

Fig. 14. Wavelet scalogram of estimated heat flux at the position of z = 30 mm at power input of 0.5 W, 2,5 W, and 4.5 W.

the intermittent oscillation of vapor/liquid meniscus of the working fluid in the tubes as shown in Fig. 5. The dependence of *cvt* on the z-direction position varied along the tubes: the dependency for the middle tubes (ch6, 7, and 8) was lower than that for the other edge tubes. Even at high power input (2.5 W and 4.5 W), the *cvt* decreased to less than 1.5 for most of the tubes, but the edge tubes still showed higher *cvt* than that of the middle tubes. It was because the fluid in this area did not often flow through the tubes in the condenser from one tube to other tube as it happened in the central tubes. This difference was probably caused by the fluids in the T-joint, the valve, and the tube between them. Since the PHP in this study had a very small inner diameter of 0.32 mm, the internal volume of these three parts was almost equivalent to one-third of the total volume. They were insulated from the environment but were not heated as the evaporator and were located at the bottom. Hence, the liquid remained there, and it worked as a buffer or a reservoir to absorb the oscillation: the stopover phenomenon was more likely to occur in the edge tubes, which resulted in the larger *cvt* there throughout all power input. In other word, in the edge tubes, the perturbation effect which led the stable and continuous fluid oscillation was smaller than in the central tubes because one side of them was connected to the T-junction and the valve acting like a reservoir. Previous study reported that the single loop PHP is more likely to occur the stop-over phenomena compare to the multi-turn PHP and the increment of number of turns leads the higher level of the perturbations [33].

4.4. Frequency analysis of local heat flux

The frequency analysis was performed for the local heat transfer at every point in each tube to clarify the variations of the oscillating motions depending on the positions in the condenser. Last decade, the fast Fourier transform (FFT) was popularly employed for the PHP frequency analysis, whereas, recently, the wavelet transform has been chosen as the powerful tool to overcome the FFT's limit that is related to the difficulty in determining the dominant frequency in the large amount of the complicated transient data [26,34,35]. In this study, the wavelet transform was applied using the Morlet wavelet, which was demonstrated to be effective for transient localization [36]. The Morlet wavelet ψ for dimensionless time η is defined by the following equation.

$$\psi(\eta) = \frac{1}{\sqrt{\pi}} e^{-\frac{\eta^2}{2}} e^{i\omega_0 \eta} \tag{17}$$

where η is the non-dimensional time and ω_0 is the non-dimensional frequency. Then the Wavelet transform of a signal $y(t)$

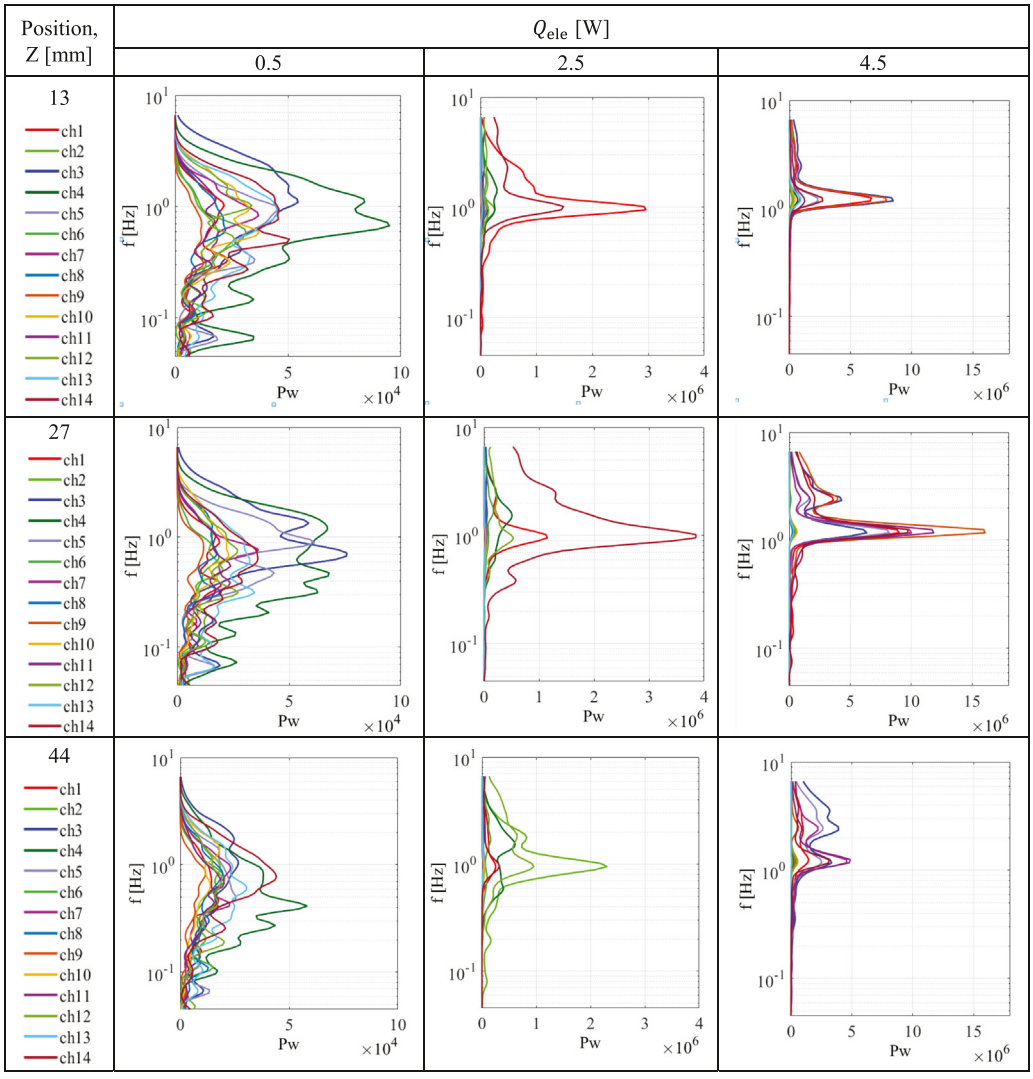

Fig. 15. Power spectrum of estimated heat flux at power input of 0.5W, 2.5W, and 4.5W.

can defined as [22]:

$$W_{\psi}(a,\tau) = \frac{1}{\sqrt{a}} \int_{-\infty}^{\infty} y(t)\psi^{*}\left(\frac{t-\tau_{sh}}{a}\right)dt \quad (18)$$

where a and τ_{sh} are the Wavelet scale and time sift, respectively, and the superscript * denotes the complex conjugate. The output of the wavelet analysis is a so-called magnitude scalogram, which represents the power related to each frequency over the sample duration, and the power spectrum, which is the time integral of the magnitude scalogram, for every frequency. Specifically, the scalogram enables to identify the main oscillation frequencies of the analysed oscillatory phenomenon, i.e., the frequencies with the greatest related power over time, while the power spectrum defines the frequency with the greatest power within the entire observation window. According to Perna et al. [35], the dominant frequency is defined here as the maximum value of the wavelet power spectrum.

The wavelet transform analysis was then performed for the local heat flux. Fig. 14 shows the scalograms at three different power inputs conditions, for an edge tube (ch1) and middle tubes (ch7 and ch8). The local heat flux showed a strong time dependency in each tube at the power input of 0.5 W, which weakened as the heat input increases, particularly in the middle tubes.

The power spectrums at three representative positions (z = 13, 27, and 44 mm) of three tubes at power input of 0.5 W, 2.5 W, and 4.5 W are shown in Fig. 15. For the low power input (0.5 W), all the tubes showed multiple peaks. The energy increased along the position on the condenser got closer to the top, but this tendency of the multiple peaks was kept. Compared to it, the dominant fluid oscillation frequency was found more clearly in higher heat input conditions. At the power input of 2.5 W, the dominant frequency was found to be around 0.95 Hz. The energy of the edge tubes oscillation was higher than the others, which resulted from the relatively high fluid-to-wall heat flux induced by the non-penetrative pulsating flow described in the previous section. At the highest power input condition (4.5 W), most of the tubes showed the peak around 1.2 Hz regardless the positions.

Similar result was found in the previous study performed frequency analysis of local heat flux [26]: the dominant frequency increased along the power input up to 1.1 Hz. In [26], it was also reported that the 80th percentile of the frequencies agrees with those evaluated by processing the pressure acquisitions. Note that the measurement target in [26] is an adiabatic section of a 14-turn PHP with FC-72 and it was measured under the microgravity conditions. Some of other studies reported the oscillation frequency of around 1–2 Hz [37,38]. Although the configuration and the test environment of the PHPs were different, there could be a possibility that the frequency reaches 1–2 Hz when the oscillation is fully activated.

5. Conclusion

The local wall-to-fluid heat flux distributions were evaluated within the condenser section of a 7-turn micro-PHP to lead to a better understanding of the fundamental governing mechanisms of PHPs, which are, so far, only partially understood. The PHP consisted of stainless-steel tubes with inner diameter of 0.32 mm and HFC-134a was filled with the filling ratio of 46% as the working fluid. The experiments were conducted at the bottom heat condition and the condenser was cooled by the natural convection. The time-space temperature maps of the condenser were acquired by high-resolution IR camera. The local heat flux was calculated by solving the IHCP at the tube wall using the temperature maps as the input data. A frequency analysis was performed to clarify the variations of the oscillating motions depending on the positions in the condenser, and the wavelet scalogram and the power spectrum was evaluated. The main outcomes are as follows.

- The fluid oscillation started at power input of 0.1 W with low amplitude which did not cover whole condenser and contains up to 5 s stopovers in whole PHP.
- Two flow regimes were observed during the fluid was continuously oscillating: random-direction flow (from 1.5 W to 3.5 W) and unidirectional flow throughout PHP with local oscillation in the tube (from 4 W to 5 W).
- The fluid motion in each tube were reflected to the local fluid-to-wall heat flux and therefore the oscillation can be successfully assessed by the heat flux.
- The coefficient of variation over space *cvs* allows the identification of the flow regime: in the case of the flow in random direction at relatively low power input (0.5 W and 2.5 W), the *cvs* has high peaks more than 2, whereas during the unidirectional flow in whole PHP at high power input (4.5 W), the peaks of the *cvs* decreased to less than 1.5.
- At all power input, the coefficient of variation over time *cvt* of edge tubes is larger than that of the central ones due to the buffer effect caused by the extra fluid in the tube junction and valve.
- The frequency analysis results also highlight the flow regime transient with the increment of the heat input: the multiple peaks were shown in each tube at low input whereas the peaks became more concentrated at high power input and increased to 1.2 Hz.

The thermographic acquisitions and IHCP resolution approach show a complete picture of working regimes of the tubular micro-PHP which is difficult to obtain by the direct measurement. The provided data will lead better understanding of micro-PHPs thermal behavior, as well as for the improvement of existing numerical models.

Declaration of Competing Interest

The authors declare that they have no known competing financial interests or personal relationships that could have appeared to influence the work reported in this paper.

Acknowledgment

This work has received funding from the European Union's Horizon 2020 research and innovation programme under the Marie Skłodowska-Curie grant agreement No 894750.

Supplementary materials

Supplementary material associated with this article can be found, in the online version, at doi:10.1016/j.ijheatmasstransfer.2022.123203.

References

[1] Mordor IntelligenceLithium-ion Battery Market - Growth, Trends, and Forecast (2019–2024) *Industry reports*, Mordor Intelligence, Hyderabad, 2019.
[2] K. Jiang, G Liao, E. Jianqiang, F. Zhang, J. Chen, E. Leng, Thermal management technology of power lithium-ion batteries based on the phase transition of materials: a review, J. Energ. Storag. 32 (2020) 10816.1–10816.25.
[3] S.S. Murshed, C.A. Nieto de Castro, A critical review of traditional and emerging techniques and fluids for electronics cooling, Renew. Sustain. Energ. Rev. 78 (2017) 821–833.
[4] Akachi, H., 1990, U.S. Patent Patent Number 4921041
[5] Akachi, H., 1993, U.S. Patent Patent Number 5219020
[6] H. Akachi, H. Polasek, P. Stluc, Pulsating heat pipes, in: Proc. 5th Intl. Heat Pipe Symp, 1996, pp. 208–217.
[7] Grover, G. M., 1966, U.S. Patent, Patent Number 3229759.

[8] F. Gerasimov, Y.F. Maidanik, G T Shchegolev, G.A. Filippov, L.G. Starikov, V.M. Kiseev, Y.E. Dolgirev, Low-temperature heat pipes with separate channels for vapor and liquid, J. Eng. Phy. Thermophy. 28 (6) (1975) 683–685.
[9] Y. Zhang, A. Faghri, Advances and unsolved issues in pulsating heat pipes, Heat Transf. Eng. 29 (1) (2008) 20–44.
[10] X. Han, X. Wang, H. Zheng, X. Xu, G. Chen, Review of the development of pulsating heat pipe for heat dissipation, Renew. Sustain. Energ. Rev. 59 (2016) 692–709.
[11] J. Qu, H. Wu, P. Cheng, Start-up, heat transfer and flow characteristics of silicon-based micro pulsating heat pipes, Intl. J. Heat Mass Transf. 55 (2012) 6109–6120.
[12] K.S. Yang, Y.C. Cheng, M.C. Liu, J.C. Shyu, Micro pulsating heat pipes with alternate microchannel width, Appl. Ther. Eng 83 (2015) 131–138.
[13] A. Yoon, S.J. Kim, Characteristics of oscillating flow in a micro pulsating heat pipe: fundamental-mode oscillation, Intl. J. Heat Mass Transf. 109 (2017) 242–253.
[14] A. Yoon, S.J. Kim, Understanding of the thermo-hydrodynamic coupling in a micro pulsating heat pipe, Intl. J. Heat Mass Transf. 127 (2018) 1004–1013.
[15] J. Kim, S.J. Kim, Experimental investigation on the effect of the condenser length on the thermal performance of a micro pulsating heat pipe, Appl. Ther. Eng 130 (2018) 439–448.
[16] J. Kim, S.J. Kim, Experimental investigation on working fluid selection in a micro pulsating heat pipe, Energ. Conver. Manag. 205 (2020) 112462.1–112462.13.
[17] J. Lim, S.J. Kim, A channel layout of a micro pulsating heat pipe for an excessively localized heating condition, Appl. Ther. Eng 196 (2021) 117266.1–117266.14.
[18] C. Kamijima, Y. Yoshimoto, Y. Abe, S. Takagi, I. Kinefuchi, Relating the thermal properties of a micro pulsating heat pipe to the internal flow characteristics via experiments, image recognition of flow patterns and heat transfer simulations, Intl. J. Heat Mass Transf. 163 (2020) 120415.1–120415.15.
[19] A. Faghri, Heat pipes: review, opportunities and challenges, Front. Heat Pipes 5 (2014) 1.1–1.48.
[20] N. Iwata, Y. Miyazaki, S. Yasuda, H. Ogawa, Thermal performance and flexibility evaluation of metallic micro oscillating heat pipe for thermal strap, Appl. Ther. Eng 197 (2021) 117342.1–117342.12.
[21] A. Takawale, S. Abraham, S. Sielaff, P.S. Mahapatra, A. Pattamatta, P. Stephan, A comparative study of flow regimes and thermal performance between flat plate pulsating heat pipe and capillary tube pulsating heat pipe, Appl. Ther. Eng 149 (2019) 613–624.
[22] M. Mameli, M. Marengo, S. Khandekar, Local heat transfer measurement and thermo-fluid characterization of a pulsating heat pipe, Intl. J. Ther. Sci. 75 (2014) 140–152.
[23] J. Jo, J. Kim, S.J. Kim, Experimental investigations of heat transfer mechanisms of a pulsating heat pipe, Energ. Conver. Manag. 181 (2019) 331–341.
[24] T.H. Kim, E. Kommer, S. Dessiatoun, J. Kim, Measurement of two-phase flow and heat transfer parameters using infrared thermometry, Intl. J. Multi. Flow 40 (2012) 56–67.
[25] L. Cattani, D. Mangini, F. Bozzoli, L. Pietrasanta, N. Miche, M. Mameli, S. Filippeschi, S. Rainieri, M. Marengo, An original look into pulsating heat pipes: Inverse heat conduction approach for assessing the thermal behavior, Ther. Sci. Eng. Prog. 10 (2019) 317–326.
[26] L. Pagliarini, L. Cattani, F. Bozzoli, M. Mameli, S. Filippeschi, S. Rainieri, M. Marengo, Thermal characterization of a multi-turn pulsating heat pipe in microgravity conditions: Statistical approach to the local wall-to-fluid heat flux, Intl. J. Heat Mass Transf 169 (2021) 120930.1–120930.16.
[27] H. Ma, *Oscillating Heat Pipes*, ISBN: 978-1-4939-2503-2, Springer, New York, 2015 2015.
[28] mini-REFPROOP - Version 10.0, 11 May 2021 https://trc.nist.gov/refprop/MINIREF/MINIREF.HTM sited at.
[29] L. Cattani, F. Bozzoli, P. Vocale, M. Malavasi, L. Pagliarini, N. Iwata, Global and local performances of a tubular micro pulsating heat pipe: experimental investigation, Heat Mass Transf. (2022) in press.
[31] V.A. Morozov, *Methods For Solving Incorrectly Posed Problems*, ISBN: 978-1-4612-5280-1, Springer, New York, 1984.
[31] V. Nikolayev, M. Marengo, *Pulsating heat pipes: basics of functioning and numerical modeling*, ISBN 978-981-3234-36-9, in: J.R. Thome (Ed.), Encyclopedia of Two-Phase Heat Transfer and Flow IV, vol. 1 Modeling of Two-Phase Flows and Heat Transfer, World Scientific, Singapore, 2018.
[32] F.P. Incropera, D.P. Dewitt, T.L. Bergman, A.S. Lavine, in: Funramentals of Heat and Mass Transfer, Sixth Ed., John Wiley & Sons, Hoboken, 2005, p. 931. ISBN: 978-0-4708-8145-3.
[33] S. Khandekar, M. Groll, An insight into thermo-hydrodynamic coupling in closed loop pulsating heat pips, Intl. J. Ther. Sci. 43 (2004) 13–20.
[34] N. Zhao, H. Ma, X. Pan, Wavelet analysis of oscillating motions in an oscillating heat pipe, Proc. ASME Intl. Mech. Eng. Cong. and Exp. 10 (2011) 545–549.
[35] R. Perna, M. Abela, M. Mameli, A Mariotti, L. Pietrasanta, M. Mameli, M. Marengo, S. Filippeschi, Flow characterization of a pulsating heat pipe through the wavelet analysis of pressure signals, Appl. Ther. Eng. 171 (2020) 115128.1–115128.13.
[36] Torrence, C. and Compo, G. P., 1998, *Bulletin of American Meteorological Society*,79(1), pp.61-78.
[37] G. Spinato, N. Borhani, J.R. Thome, Understanding the self-sustained oscillating two-phase flow motion in a closed loop pulsating heat pipe, Eng 190 (2015) 889–899.
[38] J.S. Kim, N.H. Bui, H.S. Jung, W.H. Lee, The study on pressure oscillation and heat transfer characteristics of oscillating capillary tube heat pipe, KSME Intl. J. 17 (10) (2003) 1533–1542.